Plant Phenomics 7 (2025) 100060

Contents lists available at ScienceDirect

Plant Phenomics

journal homepage: www.sciencedirect.com/journal/plant-phenomics

Research Article

# Self-adaptive individual tree modeling based on skeleton graph optimization and fractal self-similarity

Zhenyang Hui [a,b,c,*], Yating He [a,b,c], Shuanggen Jin [d,e], Wenbo Chen [a,b,c], Penggen Cheng [a,b,c], Yao Yevenyo Ziggah [f]

[a] National Key Laboratory of Uranium Resources Exploration-Mining and Nuclear Remote Sensing, East China University of Technology, Nanchang, 330013, China
[b] School of Surveying and Geoinformation Engineering, East China University of Technology, Nanchang, 330013, China
[c] Jiangxi Key Laboratory of Watershed Ecological Process and Information, East China University of Technology, Nanchang, 330013, China
[d] School of Surveying and Land Information Engineering, Henan Polytechnic University, Jiaozuo, 454000, China
[e] Shanghai Astronomical Observatory, Chinese Academy of Sciences, Shanghai, 200030, China
[f] Faculty of Mineral Resources Technology, University of Mines and Technology, Tarkwa, Ghana

ARTICLE INFO

*Keywords:*
Individual tree modeling
Skeleton points
Graph optimization
Fractal self-similarity

ABSTRACT

Three-dimensional tree modeling is crucial for forest ecological applications. However, building accurate individual tree models still faces unresolved challenges, such as wrongly connected branches within the canopy and poor quality modeling results when dealing with tree points containing data gaps. To address these issues, this paper proposes an in-novation method for individual tree modeling based on skeleton graph optimization and fractal self-similarity. In this paper, the skeleton points are initially extracted through the Laplacian-based contraction and the farthest distance spherical sampling. To centralize the extracted skeleton points within each point set, a method for skeleton points adjusting and optimization is presented, which helps achieve centralized skeleton points, particularly in cases with incomplete branch points. Additionally, instead of using Euclidean distance or its square as edge weight, the paper proposes a novel edge weight definition, which ensures the construction of correctly connected skeleton lines, especially for branches within the canopy. To improve fidelity and robustness against outliers, fractal self-similarity is first applied in this paper to refine individual tree models and achieve better modeling results. The effectiveness of the pro-posed method is evaluated using 29 individual trees of different structure characteristics with known harvest volumes. Experimental results demonstrate that this method achieves tree volumes closest to the referenced values, with a relative mean deviation of 0.01 % and a relative root mean square error of 0.09 %. Moreover, the concordance correlation coefficient of the proposed method is 0.994, outperforming two classical individual tree modeling methods, TreeQSM (Quantitative Structure Model) and AdQSM, based on five accuracy indicators.

## 1. Introduction

Trees play a vital role in maintaining ecological function, biodiversity, and the overall well-being of the planet [1–6]. The use of high-precision and high-fidelity tree models can greatly enhance the realism and immersion in the digitization process of forestry [7–9]. Additionally, three-dimensional (3D) tree models are essential components of virtual ecological landscapes and natural scenery [10,11]. Accurate 3D tree models are also valuable for calculating and predicting important tree parameters such as diameter at breast height (DBH) [12], above ground biomass (AGB) [13–15], wood volume [16–19], and tree species identification [20–22]. Therefore, constructing 3D tree models holds significant theoretical and practical value.

With the rapid development of LiDAR (Light Detection And Ranging) technology, it has become one of the main methods for modeling individual trees [23]. In order to build accurate individual tree models, most existing studies utilize cylinders as primitives to create the 3D models [24,25]. The methods for tree topological structure can be classified into two categories: cluster segmentation-based and skeleton extraction-based approaches [26]. Cluster segmentation-based methods typically segment point clouds into different clusters [27], which are then connected based on neighbor relations to form the tree topological

* Corresponding author. National Key Laboratory of Uranium Resources Exploration-Mining and Nuclear Remote Sensing, East China University of Technology, Nanchang, 330013, China.
*E-mail addresses:* huizhenyang2008@ecut.edu.cn, huizhenyang2008@163.com (Z. Hui).

https://doi.org/10.1016/j.plaphe.2025.100060
Received 12 March 2025; Received in revised form 8 May 2025; Accepted 26 May 2025
Available online 1 June 2025

structure. For example, Xu et al. [28] segmented raw point clouds into several bins using a graph-cut strategy based on shortest path length and adjacency information within each subgraph. They achieved the tree skeleton by connecting central points within each bin. Similarly, Delagrange et al. [29] obtained branch level sets by generating subgraphs and selected central points within each level set as skeleton nodes.

Raumonen et al. [30] segmented tree points into a series of cover sets. Then, they combined the neighboring relationships among these cover sets to cluster them as different branches. These branches formed the topological tree structure and could be approximated as cylinders with varying radius and orientation. Hackenberg et al. [31] proposed an open-source approach called SimpleTree. In their method, a sphere is used to extract a sub point cloud. Within each sub point cloud, and the random sample consensus (RANSAC) algorithm was applied within each sub point cloud to fit a circle. The circle center served as the end point and the sphere center served as the start point, while the circle radius represented the cylinder radius. Yan et al. [32] first employed a variational k-means clustering approach to partition the point cloud into connected subclusters. They then constructed an adjacency graph to identify tree branches. Finally, they revised the individual tree model using the B-spline method. Similarly, Li et al. [33] also used the k-means clustering method to detect wood segments and extracted skeleton nodes using a breadth-first search approach. Ai et al. [34] sliced the tree points and utilized mean-shift and principal component analysis algorithms to extract skeleton nodes for each slice. Hui et al. [35] first classified wood and leaf points, then proposed a joint neigh-boring growing method to segment wood points into different object primitives that could be fitted as cylinders. The topological branch structure was established through spatial connectivity analysis in their method. In their method, the topological branch structure can be built according to spatial connectivity analysis. Similarly, Li et al. [36] initially classified thick branch points, which were further over-segmented into several whorl-segments that were used as skeleton nodes after shrinking. Li et al. [37] segmented tree points into pieces, considering the centers of each piece as initial skeleton points that were interpolated to obtain a complete tree skeleton.

In contrast to cluster segmentation-based methods, skeleton extraction-based methods do not require the segmentation of point clouds into clusters or subsets. Instead, these methods directly obtain the skeleton from the raw point clouds. For example, Au et al. [38] calculated the Laplacian matrix based on the neighborhood information of the point cloud. The contraction and attraction weights of the matrix were updated in each iteration to achieve contraction. The iteration continued until a zero-volume skeletal shape was achieved. Cao et al. [39] improved this method without performing surface reconstruction. Su et al. [40] applied this strategy to construct tree models. To obtain the final curve skeleton, an incomplete graph was first built using sampling points. By refining the graph, intact shapes of tree models could be obtained. Wang et al. [41] extracted the initial tree skeleton by building a distance minimum spanning tree. To fill data gaps caused by occlusion, stretching directions of branches were defined. Finally, a Laplacian function was used to refine the tree skeleton. Xu et al. [42] proposed a hierarchical modeling method using mobile LiDAR point clouds. In their method, a connected undirected graph was first constructed using raw tree points. Subsequently, the Dijkstra algorithm was employed to generate initial skeletons, which were further optimized based on line connectivity and morphological characteristics of the tree. Wu et al. [43] extracted a coarse skeleton by organizing raw points using k-dimensional trees. In this step, the searching radius was self-adaptively calculated based on linear degree and plane degree indicators. After skeleton thinning and noise filtering, the final tree skeleton could be obtained. Sun et al. [44] first classified wood points from leaf points and then applied voxel thinning for fast skeleton extraction. The initial skeleton was revised using a breakpoint connection algorithm. Cárdenas et al. [15] directly extracted skeletons from the geodesic graph, formed by merging neighborhood-based and minimum spanning tree (MST)-based graphs.

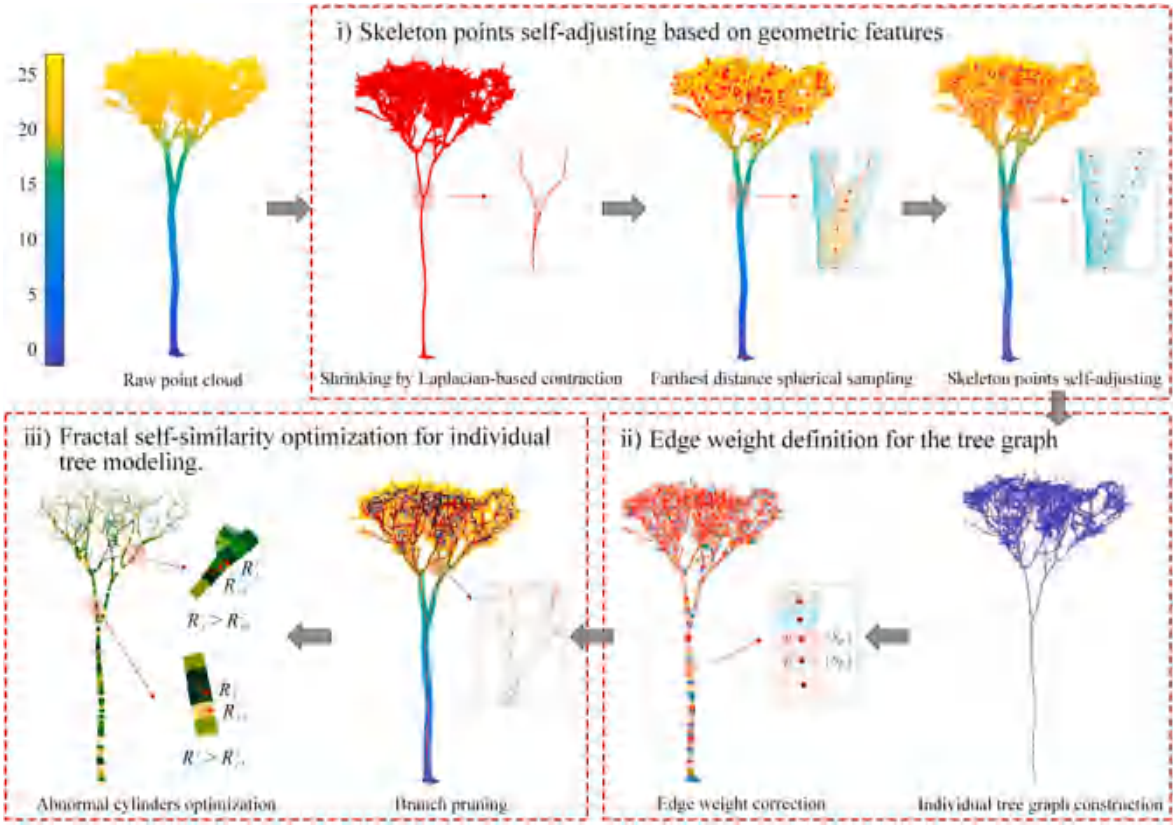


**Fig. 1.** Flowchart of the proposed method.

In summary, although many methods for 3D tree modeling have been proposed, there are still three problems that need to be further addressed. Firstly, most individual tree modeling methods require the separation of wood points from leaf points, which remains an unresolved issue. Secondly, constructing a correct topological structure of branches within the crown region, especially when dealing with incomplete point clouds caused by single-scan mode or branch self-occlusion, is still challenging. Finally, individual tree modeling results are susceptible to outliers, resulting in the creation of abnormal branches. Thus, further research is needed to achieve self-adaptive modeling and enhance the robustness of modeling methods.

To solve these challenges, this paper proposed a three-dimensional tree modeling method based on skeleton graph optimization and fractal self-similarity. In this paper, three main contributions have been made as follows:

i) A self-adjusting strategy for skeleton points was developed to centralize the points and improve the robustness of skeleton point extraction, particularly when dealing with incomplete branch points.
ii) A novel definition of edge weights was proposed, which helped in extracting accurate skeleton lines and preventing the construction of incorrect topology among branches.
iii) Fractal self-similarity is first applied in the tree modeling, which aids in constructing high fidelity 3D tree models.

## 2. Materials and methods

The flowchart of the proposed method is illustrated in Fig. 1. The skeleton points were initially obtained through Laplacian-based contraction and farthest distance spherical sampling. However, these skeleton points are not consistently centralized. To address this issue, we intro-duce a self-adjusting technique in this study to reposition each skeleton point at the center of its local neighborhood, thereby enhancing the robustness of skeleton point extraction, particularly in cases of incomplete points caused by occlusion. Additionally, a novel edge weight definition is proposed to facilitate the extraction of skeleton lines and prevent incorrect topology formation among branches. Moreover, we present the first application of fractal theory in optimizing three-dimensional individual tree models, leveraging fractal self-similarity to trim small branches and detect abnormal cylinder primitives. In essence, this study comprises three main steps: i) Skeleton points self-adjusting based on geometric features, ii) Edge weight definition for the tree graph, and iii) Fractal self-similarity optimization for individual tree modeling.

### 2.1. Skeleton points self-adjusting based on geometric features

As shown in Fig. 1, points shrinking are first conducted to the raw individual tree points through Laplacian-based contraction, which aims to transform the individual tree points $P = \{p_i\}$ into a zero-volume point set [39]. By conducting the farthest distance spherical sampling process, the skeleton points can be achieved as shown in Fig. 2 (a). However,

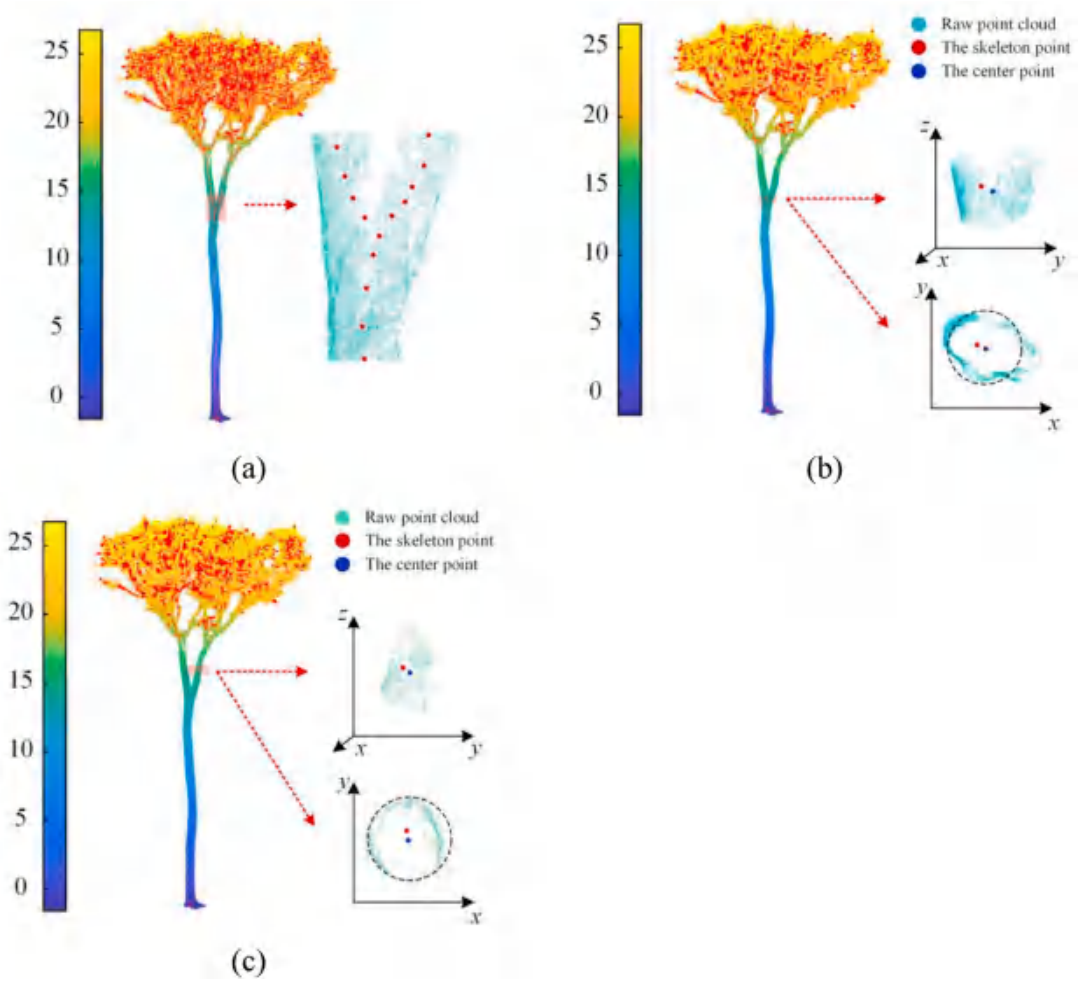


**Fig. 2.** Skeleton points deviated from their central positions. (a) Extracted skeleton points through Laplacian-based contraction and the farthest distance spherical sampling. (b)Skeleton points at the bifurcation. (c) Skeleton points at the branch with data gap.

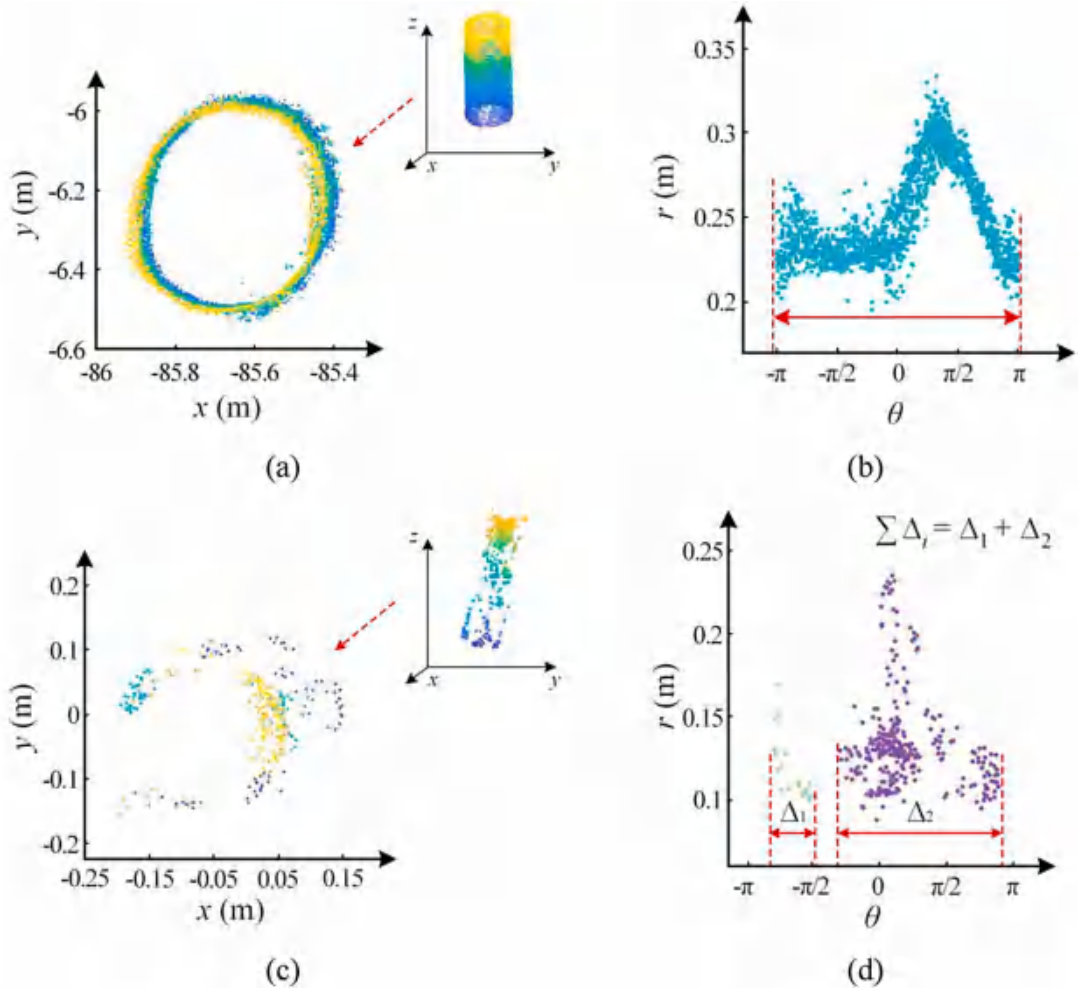


**Fig. 3.** Reliable and indeterminate skeleton points identification. (a) Complete cross-section points projected onto x-y coordinates. (b) Complete cross-section points transformed to polar coordinates. (c) Incomplete cross-section points projected onto x-y coordinates. (d) Incomplete cross-section points transformed to polar coordinates.

from Fig. 2 (a), it can be found that the Laplacian-based contraction process may not ensure that the extracted skeleton points are located at the center of each object primitive, especially when dealing with point clouds at bifurcations. This is due to the fact that during the contraction process, stronger contraction constraints are generally applied to thicker regions, causing the neighboring vertices of thinner regions to move away from their centers, as shown in Fig. 2 (b) [38]. Furthermore, when the branch points are incomplete, the contracted skeleton points often deviate from their central positions, as demonstrated in Fig. 2 (c). Therefore, it is necessary to adjust the extracted skeleton points in order to make them centralize their corresponding object primitive.

In this paper, the skeleton points are initially classified into two categories to distinguish between skeleton points contracted from complete point clouds and those contracted from incomplete points. These categories are referred to as 'reliable skeleton points' and 'indeterminate skeleton points', respectively. Indeterminate skeleton points are detected by transforming the points into polar coordinates. As depicted in Fig. 3 (a) and (b), when all cross-section points are present, the transformed polar coordinates should form a connected range along the angular domain $[-\pi,\pi]$. Conversely, when some cross-section points are missing (Fig. 3 (c)), the corresponding transformed polar coordinates cannot cover the entire angular domain. Therefore, to differentiate between reliable and indeterminate skeleton points, the transformed polar coordinates are clustered using a density-based spatial clustering method [45]. Subsequently, the effective domain ($\sum \Delta_i$) can be calculated by summing together the connected parts, as illustrated in Fig. 3 (d). If the effective domain covers more than two thirds of the angular domain $[-\pi, \pi]$, that is $\sum \Delta_i \geq \frac{4}{3}\pi$, then the corresponding skeleton point is considered a reliable skeleton point. Otherwise, it is identified as an indeterminate skeleton point.

In terms of the reliable skeleton points, their central positions can be adjusted using the least square fitting towards the projected points. In terms of the indeterminate skeleton points, since they are formed by incomplete points, their positions generally need to be adjusted gradually. As shown in Fig. 4 (a), $p_1$ and $p_2$ are two successive reliable skeleton points, $p_3$ is an indeterminate skeleton point. The angle of $p_1p_2$ and $p_1p_3$ can be calculated as $\alpha = \langle p_1p_2, p_1p_3 \rangle$. If $\alpha$ is larger than a threshold $\gamma$, it means $p_3$ needs to be adjusted. The adjusting process is iterative. In each iteration, $p_3$ is adjusted as the central point $p_3^i$ along the perpendicular line $p_3p_3'$. The adjusting keeps iteratively until the angle $\langle p_1p_2, p_1p_3^i \rangle$ is smaller than $\gamma$. In another case, as shown in Fig. 4 (b), when two indeterminate skeleton points ($p_2$ and $p_3$) are followed one reliable skeleton point ($p_1$), these two indeterminate skeleton points can be adjusted gradually. Firstly, $p_2$ can be adjusted as $p_2^i$ based on the angle $\langle p_1p_4, p_1p_2 \rangle$. Then, $p_2^i$ can be seen as a reliable skeleton point and $p_3$ can be adjusted according to the adjusting strategy mentioned above.

### 2.2. Edge weight definition for the tree graph

After adjusting the skeleton points to be at the center of each point

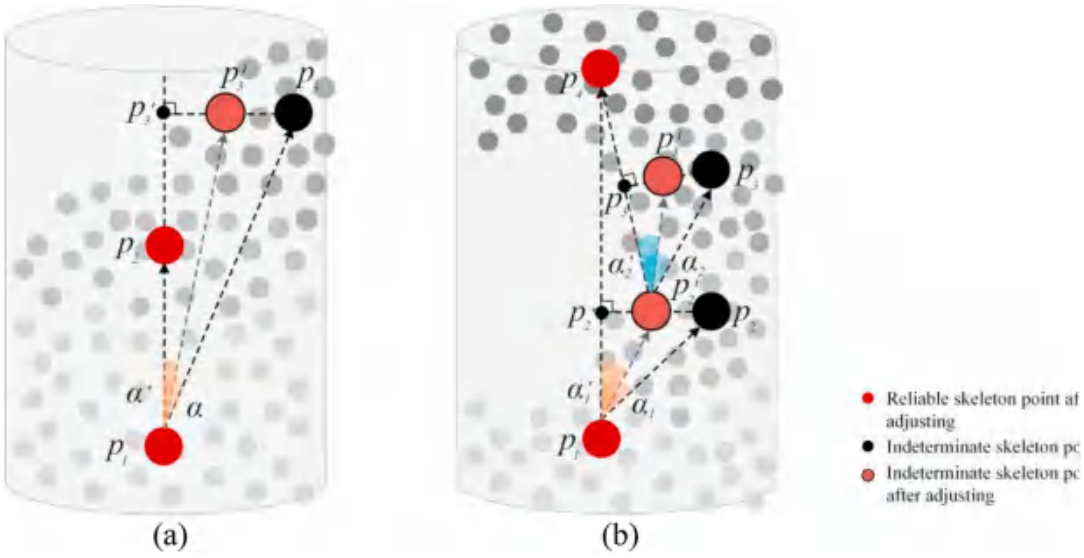


**Fig. 4.** Indeterminate skeleton points adjusting. (a) Two reliable skeleton points followed by one indeterminate skeleton point. (b) One reliable skeleton point followed by two indeterminate skeleton points.

set, the skeleton lines can be extracted using the Dijkstra shortest path principle. However, due to scanning view or branch self-occlusion, there are often data gaps among branches. This results in an unconnected individual tree graph with many separated branches, as shown in Fig. 5 (a).

To address this issue, this paper first identifies the connected components within the unconnected graph (Fig. 5 (a)). Each connected component represents a sub-graph, as shown in Fig. 5 (b). The sub-graph containing the tree root is considered the backbone sub-graph, representing the main stem of the tree. The other sub-graphs typically represent separated branches. To create a complete individual tree graph, these separated branch sub-graphs need to be connected to the backbone stem sub-graph. In this paper, this connection is conducted gradually based on the importance of each sub-graph, which is calculated based on the number of nodes within the sub-graph. As shown in Fig. 5 (b), the six branch sub-graphs are ranked as I, II, III, IV, V, and VI according to their importance. The I sub-graph is then connected to the backbone sub-graph by calculating the Dijkstra's shortest path distance between the root node of the I sub-graph and the closest nodes within the backbone sub-graph, as shown in Fig. 5 (c). The other separated sub-graphs are gradually connected until a complete individual tree graph is obtained, as shown in Fig. 5 (d).

To accurately represent branch structure details, skeleton lines need to be extracted from the constructed individual tree graph. Many researchers achieve this by calculating the Dijkstra's shortest path distance between each node within the graph and the tree root node. The setting of edge weight metrics during this process is crucial to the results of the skeleton lines. Previous studies typically set the edge weight as the Euclidean distance or square of Euclidean distance between neighboring skeleton nodes [26,28,42,46]. However, this approach has two drawbacks. Firstly, the extracted skeleton nodes often fail to accurately represent branch structure details, especially in the presence of outliers. This results in unreliable skeleton line extraction based on incorrectly detected skeleton points. Secondly, regardless of whether the Euclidean distance or square of Euclidean distance is used for edge weight calculation, the skeleton nodes are prone to incorrect connections based on shortest path calculations, particularly within the canopy region. This can be seen in the red rectangle areas (I, II and III) shown in Fig. 6 (a) and (b), where artificial branches are formed due to incorrect connections among skeleton nodes. The main reason for this is that Euclidean distance or square of Euclidean distance among the skeleton nodes cannot adequately reflect true branch topological structures.

To solve this problem, this paper defines the edge weight as the closest distance among the contracted point sets. As mentioned above, each skeleton point represents a contracted point set after the Laplacian-based contraction process. This means that several neighboring points are contracted into a single skeleton node. In Fig. 7 (a), $p_i$ and $p_j$ are two skeleton nodes, while the pink points ($\{S_{p_i}\}$) and orange points ($\{S_{p_j}\}$) are their corresponding contracted point sets. Instead of directly calculating the Euclidean distance or square of Euclidean distance between $p_i$ and $p_j$, this paper calculated the edge weight according to Eq. (1).

$$\begin{cases} p_j = \{p_j \mid \|p_i, p_j\| = \min, p_j \in \textit{skeleton nodes}\}, \\ w(p_i, p_j) = \min\limits_{p_i \in \{S_{p_i}\}} \|p_i, p_j\| \\ \qquad\qquad\quad p_j \in \{S_{p_j}\} \end{cases} \tag{1}$$

Eq. (1) indicates that the closest skeleton node $p_j$ to $p_i$ is first determined. Then, the contracted point sets $\{S_{p_i}\}$ and $\{S_{p_j}\}$ corresponding to $p_i$ and $p_j$ are identified based on a mapping relationship. The edge weight between $p_i$ and $p_j$ is defined as the shortest distance between any points from $\{S_{p_i}\}$ and any points from $\{S_{p_j}\}$. Once all the edge weights are calculated, Dijkstra's shortest path algorithm is applied to extract the final skeleton lines. Fig. 7 (b) shows the skeleton line extraction results using the proposed method. Compared to Fig. 6 (a) and Fig. 6 (b), the proposed method is able to accurately extract the skeleton lines and effectively avoid introducing artificial branches.

### 2.3. *Fractal self-similarity optimization for individual tree modeling*

Fractal geometry was first defined by Mandelbrot [47]. In fractal theory, fractals believe that the structure or shape of an object shows a similarity to the whole when observing at different scales [48]. The three-dimensional structure of trees owns typical fractal geometric characteristics.

Therefore, when creating a three-dimensional tree model, it is important to consider its fractal geometric characteristics. However, the presence of leaf points or outliers often leads to the creation of numerous small and short branches in the constructed tree model, which can make it appear unnatural. In order to improve the tree model, this study proposes a method for pruning these small and short branches based on their fractal geometric characteristics. According to fractal geometry, the local details of a fractal are similar to its overall shape. As a result,

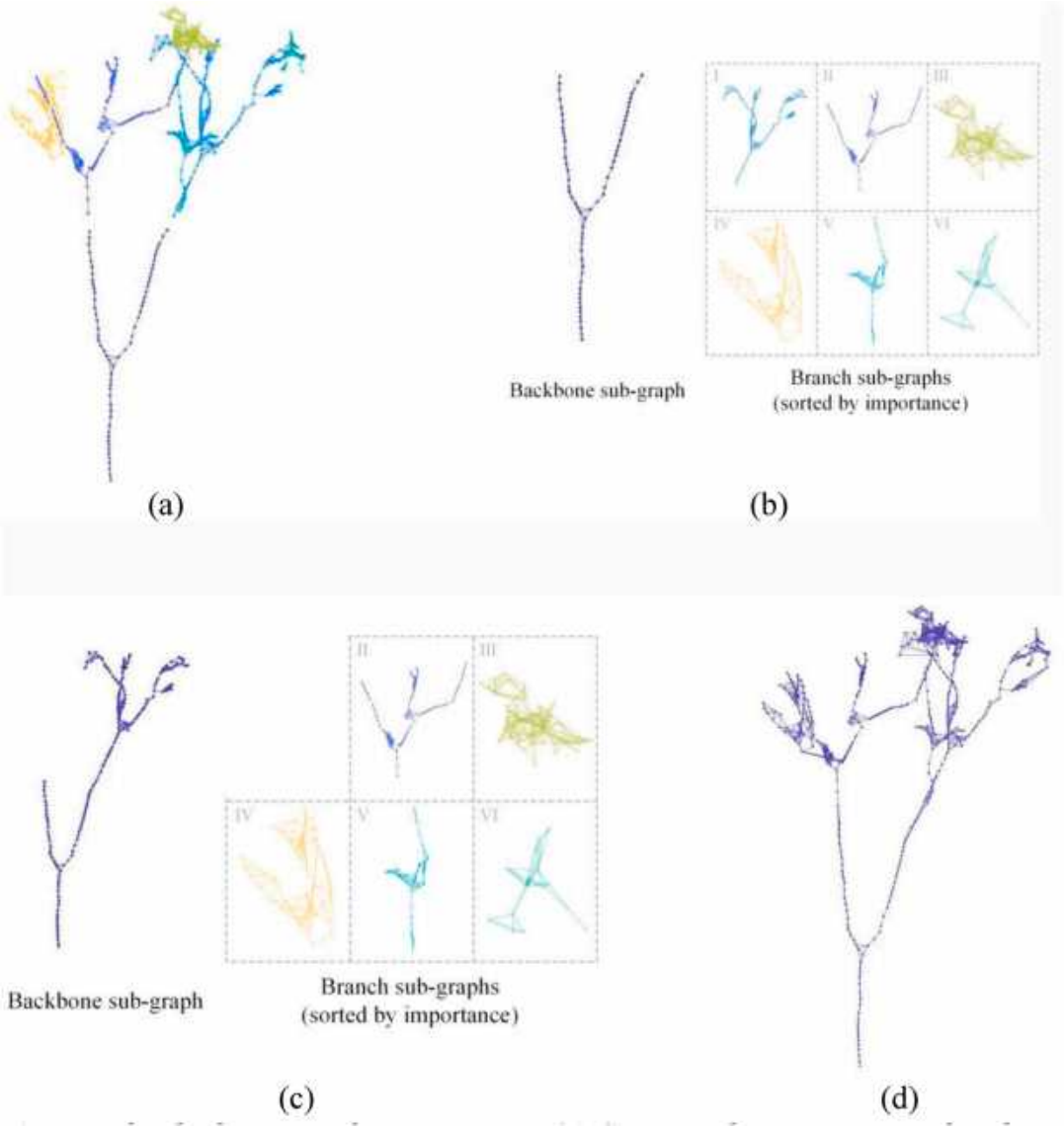


**Fig. 5.** Individual tree graph construction. (a) Connected components within the tree graph. (b) Backbone sub-graph and branch sub-graphs. (c) Branch sub-graphs are connected to the backbone sub-graph gradually. (d) The final connected individual tree graph.

this study calculates the length ratio of branches at different levels, which is defined as Eq. (2).

$$\eta(i,j)=\frac{l(i,j)}{l(i-1,j)},\ \begin{matrix} i\in[1,N] \\ j\in[1,M] \end{matrix} \tag{2}$$

where $N$ is the number of branch levels, $M$ is the number of branches at i-th level. $l(i,j)$ means the length of j-th branch at i-th level. $l(0,1)$ represents the length of the stem. In general, $\eta(i,j)$ of the branch of the same level should be similar. Thus, if $\eta(i,j)$ is distinctly small, its corresponding branch should be pruned. The threshold for this is defined as Eq. (3).

$$th(i)=mean(\eta(i,j))+std(\eta(i,j)),j\in[1,M] \tag{3}$$

where $mean(\cdot)$ represents the average value, while $std(\cdot)$ means the standard deviation value.

In addition to these small or short branches, there are also some abnormal cylinders that are generated based on incorrectly calculated radii. Clearly, the radii of these abnormal cylinders should be optimized. Generally, the cylinder radius becomes smaller and smaller along the direction of branch growth. Furthermore, the cylinder radii of neighboring nodes typically have a power-law relationship with their corresponding branch lengths, which can be represented by Eq. (4).

$$\left(\frac{R_j^i}{R_{j-1}^i}\right)=\left(\frac{l_j^i}{l_{j-1}^i}\right)^{\tau_j^i} \tag{4}$$

where $R_j^i$ and $R_{j-1}^i$ are the cylinder radiuses of child and parent nodes at $i$-th branch level, respectively. $l_j^i$ and $l_{j-1}^i$ are the lengths of branches followed each node. $\tau_j^i$ is the radius coefficient for the $j$-th cylinder at $i$-th branch level.

According to fractal theory, there is self-similarity between the branches. Hence, the ratio of cylinder radii between child and parent nodes will be similar at the same level of the branches. Consequently, the radius coefficient $\tau_j^i$ can be calculated using the correct cylinder radii and can be expressed as Eq. (5).

$$\tau_j^i=\log\left(\frac{R_j^i}{R_{j-1}^i}\right)\Big/\log\left(\frac{l_j^i}{l_{j-1}^i}\right) \tag{5}$$

It should be noted that only correct cylinder radii at each level of the

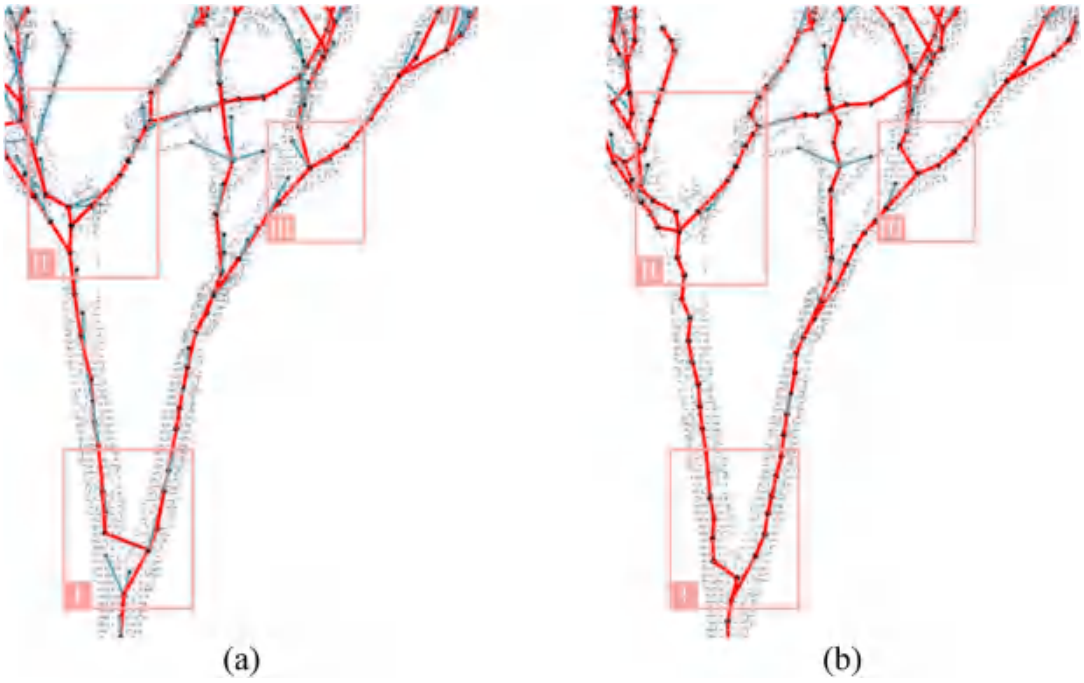


**Fig. 6.** Wrongly extracted skeleton lines. (a) Edge weight is defined as the Euclidean distance between nodes. (b) Edge weight is defined as the square of Euclidean distance between nodes.

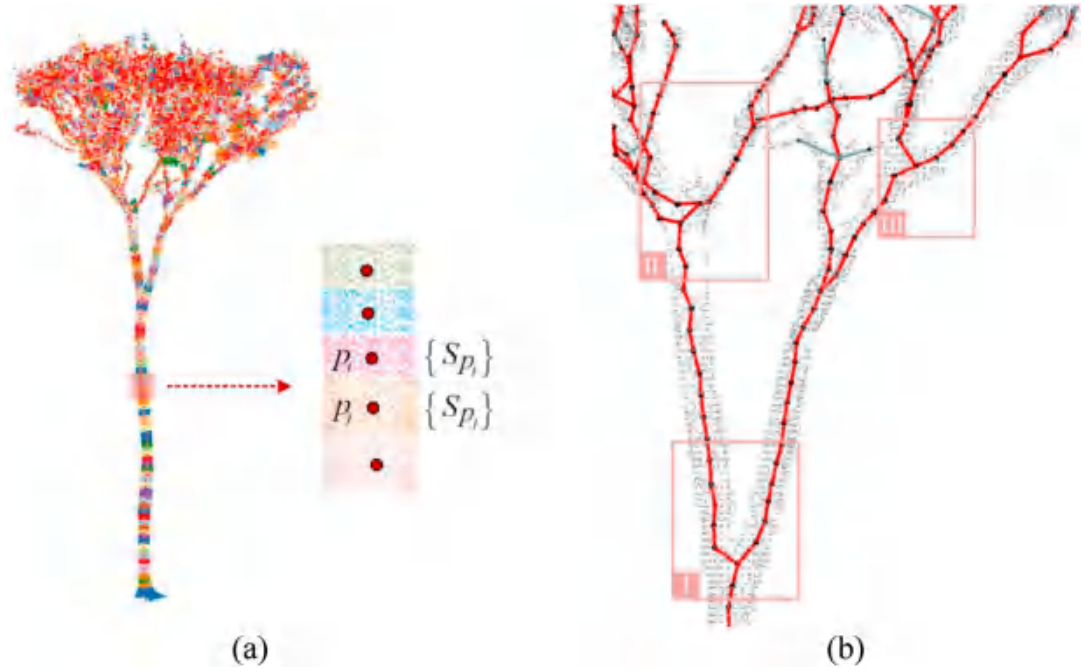


**Fig. 7.** Edge weight setting based on the shortest distance among contracted point sets. (a) Edge weight setting between skeleton nodes $p_i$ and $p_j$. (b) The skeleton lines extraction results using the proposed method.

branch were considered when calculating $\tau_j^i$. A cylinder was identified as an abnormal cylinder if its radius was larger than that of its parent node. Once all $\tau_j^i$ for the correct cylinders were calculated, $\tau^i$ for the $i$-th branch could be obtained as the mean value. That is $\tau^i = \frac{1}{K}\sum_{j=1}^{K}\tau_j^i$.

In this paper, each level of the branch has a different $\tau^i$. When $\tau^i$ is calculated, the abnormal cylinder radius can be corrected based on Eq. (6). If the abnormal cylinder belongs to a branch node where only one child cylinder is followed by another, then the abnormal cylinder radius will be optimized based on $\tau^i$. If the abnormal cylinder belongs to a bifurcate node where two or more child cylinders are followed by another, then the abnormal cylinder radius will be optimized based on the minimum value of $\{\tau_j^i\}$. This is because $\left(\frac{l_j^i}{l_{j-1}^i}\right)$ is generally smaller than 1, making $f(x) = \left(\frac{l_j^i}{l_{j-1}^i}\right)^x$ a monotonically decreasing function when $x \geq 0$. Generally, the cylinder radius should be larger if the cylinder is located at the bifurcated part. Thus, the minimum value of $\{\tau_j^i\}$ is used to optimize the radius at the bifurcate node.

**Table 1**
Characteristics of the tested trees located at three forest sites [17].

| | Peruvian Site | Indonesian Site | Guyanese Site |
|---|---|---|---|
| Number of trees | 9 | 10 | 10 |
| Forest types | Lowland tropical moist Terra firme forest | Peat swamp forest | Lowland tropical moist forest |
| Mean elevation | 312m a.s.l. | 22m a.s.l. | 117m a.s.l. |
| Mean stems density | 565 stems/ha | 1314 stems/ha | 516 stems/ha |
| Mean DBH | 90.0 cm | 58.4 cm | 73.7 cm |

$$\begin{cases} R_j^i = R_{j-1}^i \left( \dfrac{l_j^i}{l_{j-1}^i} \right)^{\tau^i}, \text{branch node} \\ R_j^i = R_{j-1}^i \left( \dfrac{l_j^i}{l_{j-1}^i} \right)^{\min\{\tau_j^i\}}, \text{bifurcate node} \end{cases} \tag{6}$$

## 3. Experimental results and analysis

### 3.1. Experimental datasets

The proposed 3D individual tree modeling method was evaluated using the datasets consisted of scans from three different tropical forest sites: Peru, Indonesia, and Guyana. These sites represented various forest types, including lowland tropical moist terra firmed forest, peat swamp forest, and lowland tropical moist forest. A total of 29 individual trees were scanned at these sites using a Riegl VZ-400 terrestrial laser scanner with a wavelength of 1550 nm. The scanner had a scanning range of 100° in zenith and a scanning resolution of 0.06°. Some detailed information for tested samples was described in Table 1. Multi-scanning mode was applied to each plot, and the resulting point clouds were co-registered with an accuracy of 1 cm. All trees were harvested destructively, including their stems, buttresses, and branches. The volumes of the stem and branches (diameter >10 cm) were calculated using the Smalian formula [49], while the volume of buttresses was calculated using the triangular prism volume formula [17]. This allowed for accurately obtaining the referenced individual tree volume. Ideally, if the performance of the proposed 3D modeling method is satisfied, its corresponding volume should be similar with the referenced tree volume. Therefore, the deviation between the tree volumes obtained from the proposed method (SfQSM) and the referenced tree volumes can be used to assess its performance.

**Table 2**
Accuracy metrics of different methods.

| | TreeQSM | AdQSM | SfQSM |
|---|---|---|---|
| *md* ($m^3$) | 0.368 | 4.024 | 0.162 |
| *rmd* | 0.030 | 0.360 | 0.010 |
| *rmse* ($m^3$) | 6.214 | 5.850 | 1.023 |
| *rrmse* | 0.550 | 0.520 | 0.090 |
| *ccc* | 0.748 | 0.859 | 0.994 |

### 3.2. Experimental results

Fig. 8 display the tree volume deviations of the proposed modeling results compared to the harvested tree volumes. From Fig. 8, it can be observed that the volume deviations for trees in Indonesian Site tend to be smaller, while those for trees in Peruvian Site tend to be larger. This can be explained by the findings in Table 1. The mean diameter at breast height (DBH) of trees in the Indonesian Site (58.4 cm) is much smaller than that of trees in the Peruvian Site (90.0 cm), as shown in Table 1. Therefore, it can be concluded that larger trees tend to have a greater deviation in tree volumes when building 3D tree models. The right panel of Fig. 8 illustrates the distribution of tree volume deviations across different forest sites. It can be observed that for most trees in all three forest sites, the tree volume deviations fall between $-1$ $m^3$ and 1 $m^3$. This indicates that the proposed individual tree modeling method can achieve similar tree volumes to the harvested ones. Furthermore, the distribution of tree volume deviations suggests that the trees in the Indonesian Site tend to yield better individual tree modeling results compared to the other two forest sites.

### 3.3. Comparison and analysis

To quantitatively assess the accuracy of the proposed tree modeling method, the accuracy metrics including mean deviation (*md*), relative mean deviation (*rmd*), root mean square error (*rmse*), relative root mean

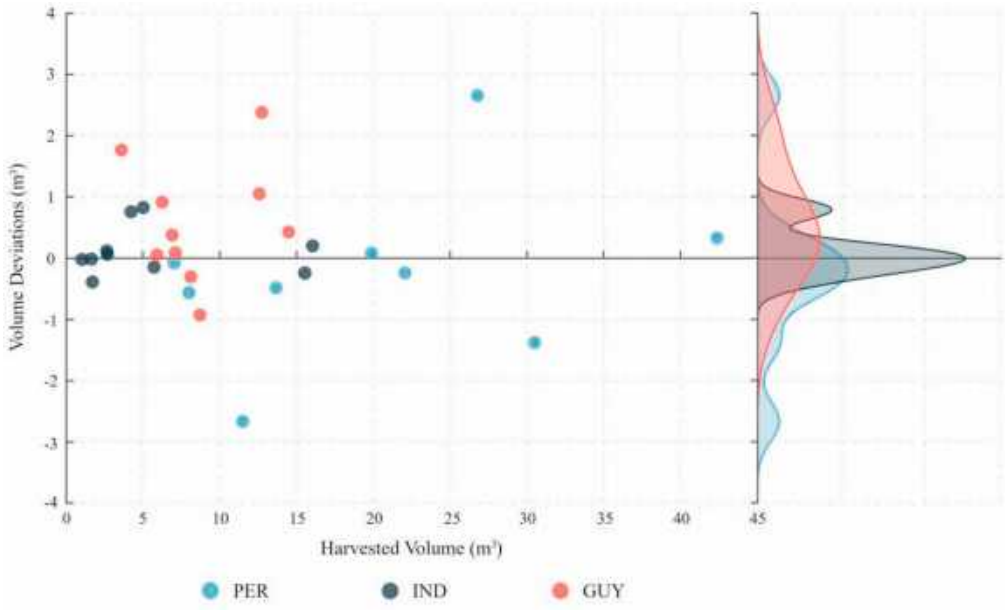


**Fig. 8.** Volume deviations of the tree modeling results and the corresponding harvested volumes.

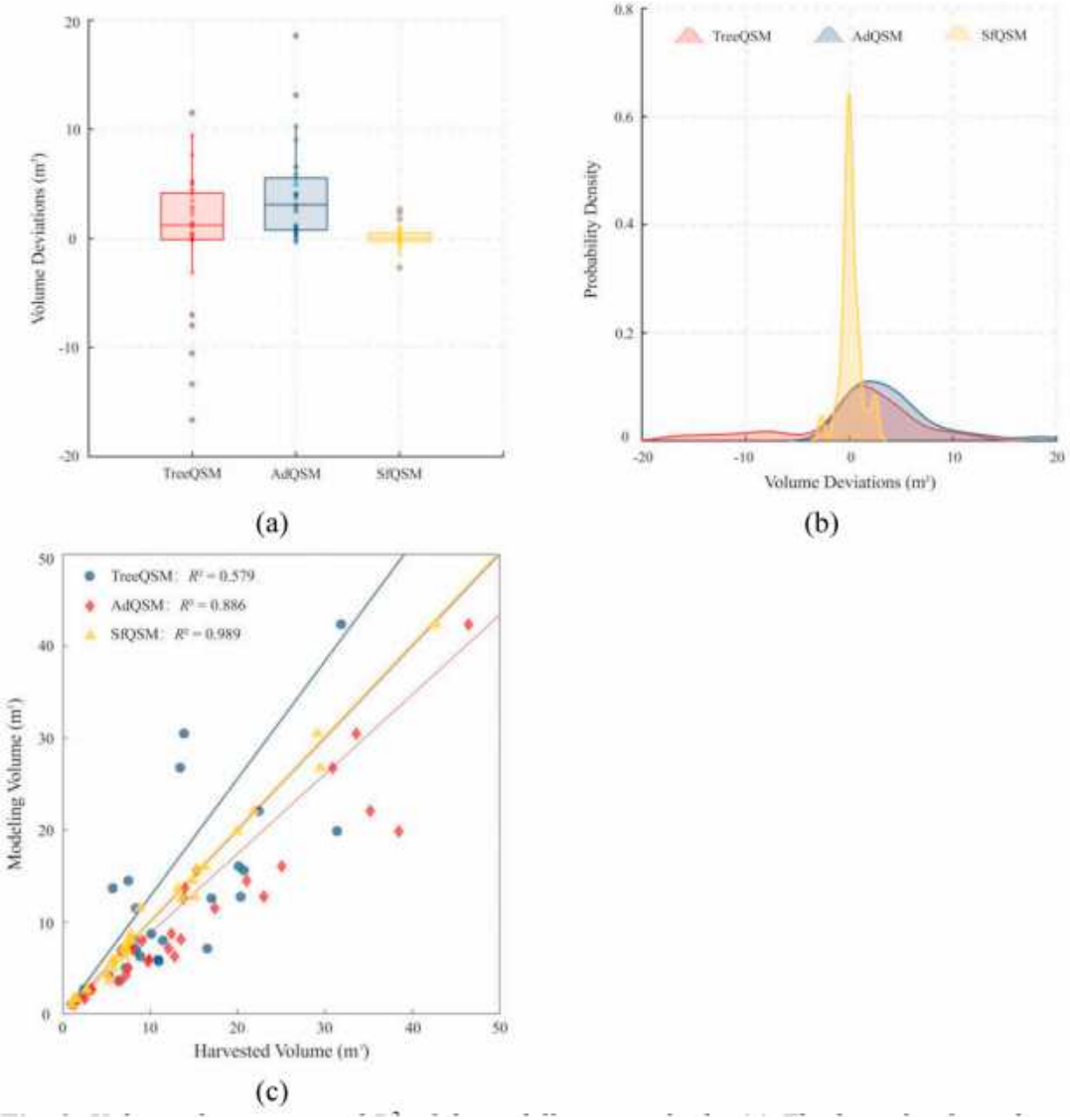


**Fig. 9.** Volume deviations and $R^2$ of three different methods. (a) The box plot for volume deviations. (b) The kernel density function distribution of volume deviations. (c) Coefficient of determination of three different methods. The blue circle represents the results by TreeQSM, the red diamond represents the results by AdQSM and the yellow triangle represents the results by SfQSM.

square error (*rrmse*), and concordance correlation coefficient (*ccc*), were calculated for assessing the individual tree modeling performance. These metrics were defined as Eqs. (7)–(11).

$$md = \sum_{i=1}^{n} \left(V_i - V_i^r\right) / n \tag{7}$$

$$rmd = md / \overline{V^r} \tag{8}$$

$$rmse = \sqrt{\sum_{i=1}^{n} \left(V_i - V_i^r\right)^2 \Big/ n} \tag{9}$$

$$rrmse = rmse / \overline{V^r} \tag{10}$$

$$ccc = \frac{2\sum_{i=1}^{n}(V_i - \overline{V})\left(V_i^r - \overline{V^r}\right)/n}{\frac{1}{n}\sum_{i=1}^{n}(V_i - \overline{V})^2 + \frac{1}{n}\sum_{i=1}^{n}\left(V_i^r - \overline{V^r}\right)^2 + (\overline{V} - \overline{V^r})^2} \tag{11}$$

where $V_i$ is the SfQSM calculated tree volume, $V_i^r$ is the corresponding harvest tree volume. $n$ is the number of trees, $\overline{V}$ is the mean value of SfQSM calculated tree volumes and $\overline{V^r}$ is the mean value of corresponding harvested tree volumes.

For comparative analysis, two open-source methods, TreeQSM and AdTree, were used. TreeQSM, proposed by Raumonen et al. [30], divides tree point clouds into small cover sets and utilizes their adjacency for connectivity analysis. The resulting connectivity between cover sets is then used for cylindrical fitting to generate individual tree models. The code for TreeQSM can be found at https://github.com/InverseTampere/TreeQSM (accessed on 10 December 2023). AdTree, proposed by Du et al. [26], obtains an initial skeleton using the Dijkstra shortest path algorithm and gradually optimizes it to obtain the final tree skeleton. Individual tree models are then obtained through cylindrical fitting. Fan et al. [23] further developed this method into an open-source tool called AdQSM, with the code available at https://github.com/GuangpengFan/AdQSM (accessed on 10 December 2023).

Table 2 presents the accuracy metrics for these three modeling methods. The proposed method (SfQSM) achieves a mean deviation of 0.162 $m^3$ and a root mean square error of 1.023 $m^3$. The relative mean deviation and relative root mean square error are 0.01 % and 0.09 %,

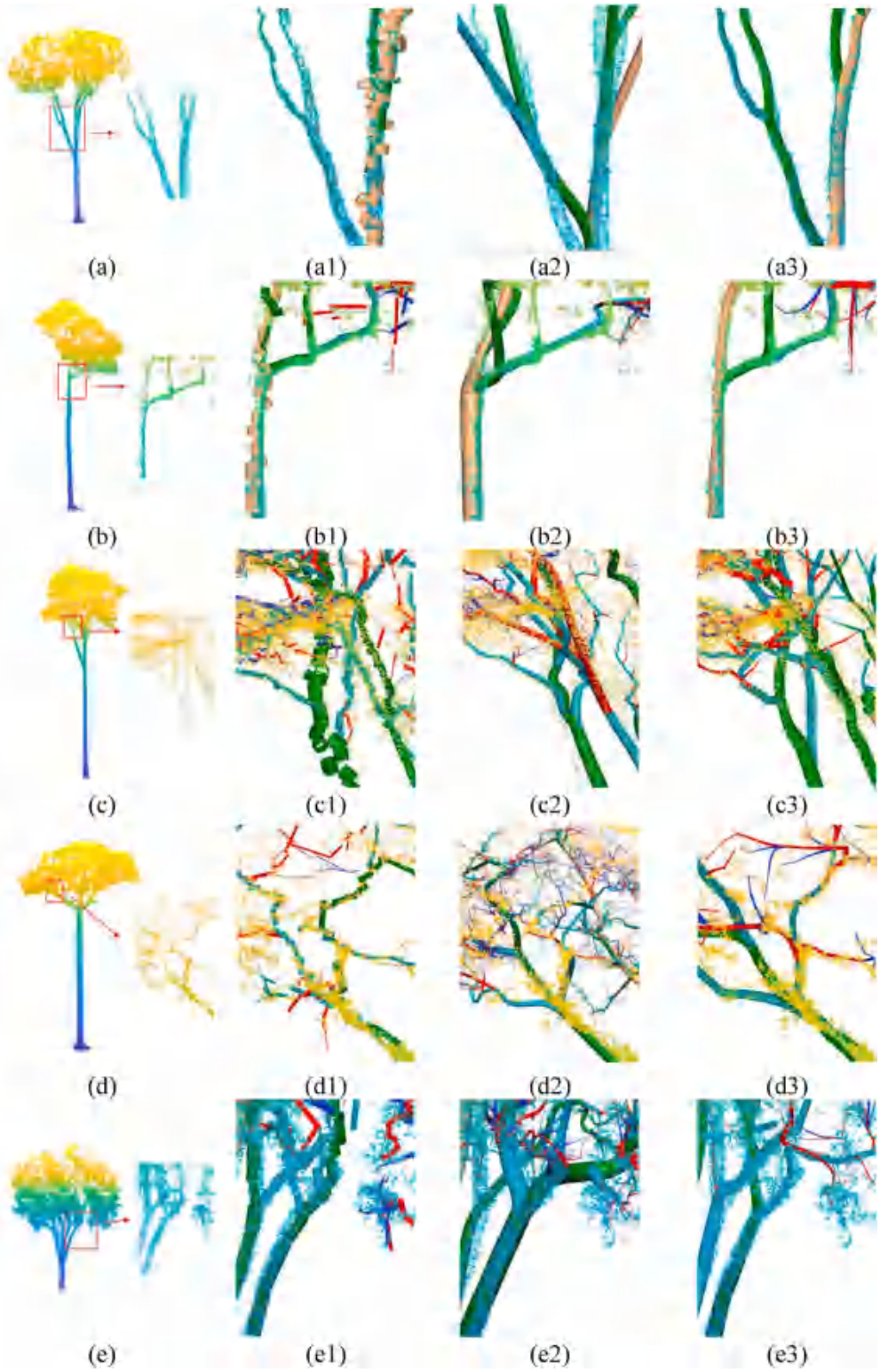


**Fig. 10.** Tree points superimposed with modeling results. The first column shows the individual tree point clouds. The second column shows the modeling results of TreeQSM for the selected tree points. The third column shows the modeling results of AdQSM for the selected tree points. The forth column shows the modeling results of the proposed method for the selected tree points.

respectively. In terms of mean deviation of tree volume, it can be observed that the mean deviation of TreeQSM is more than twice that of the proposed method (SfQSM), while the mean deviation of AdQSM is more than thirty times that of SfQSM. This indicates that the proposed method can achieve more accurate individual tree modeling results leading to more accurate tree volume estimations. Similarly, in terms of root mean square error, the root mean square error of TreeQSM is more than six times that of SfQSM, while the root mean square error of AdQSM is more than five times that of SfQSM. This demonstrates that the proposed method achieves robust individual tree modeling results

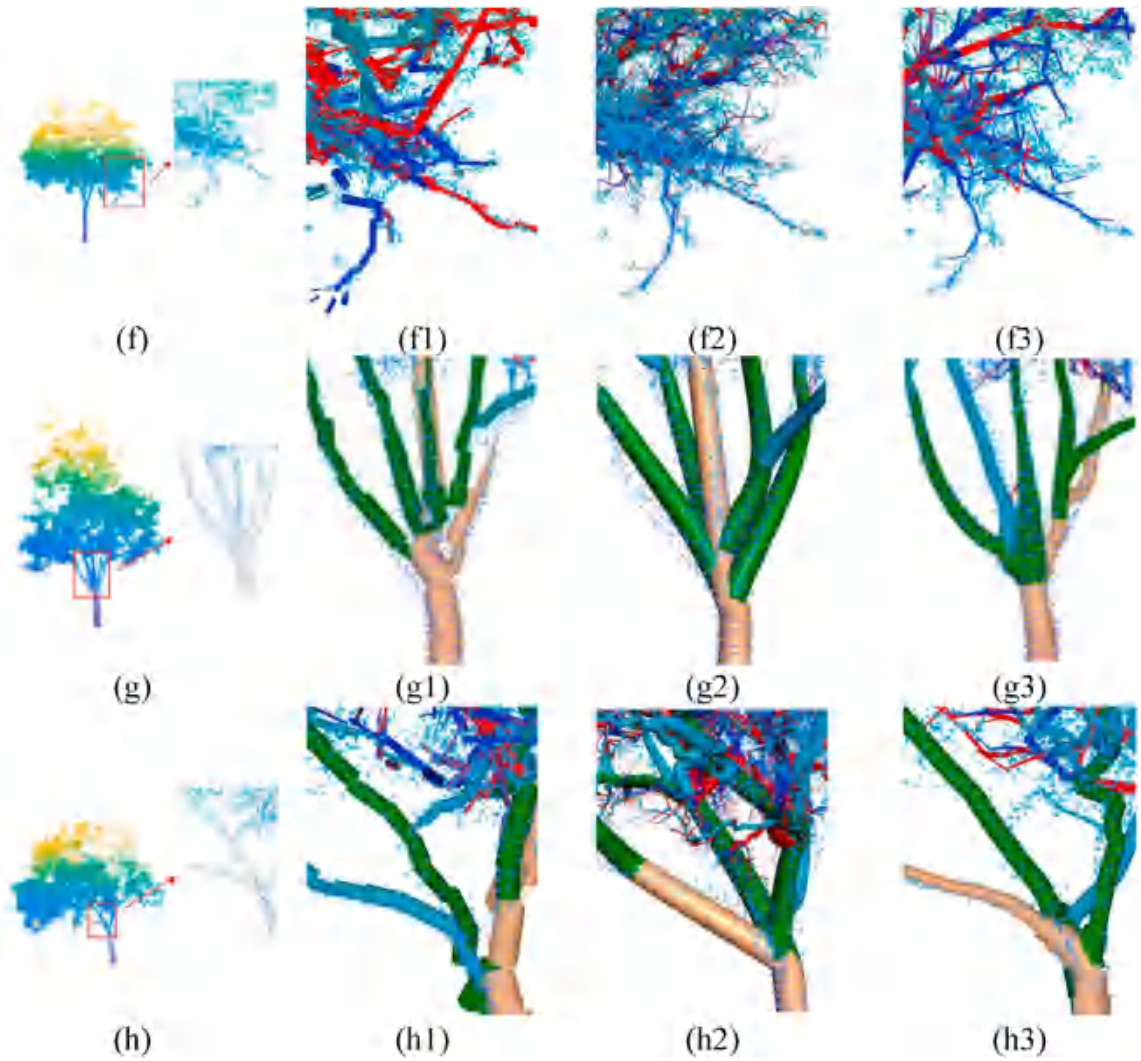


**Fig. 10.** (*continued*).

**Table 3**
Trees scanned in multi-scan mode and single-scan mode with smaller or larger data gaps.

| Samples | Height (m) | Width (m) | Scanning mode | Data gaps | Number of points |
|---|---|---|---|---|---|
| PRE08 | 27.887 | 6.464 | Multi-scan | low | 77,812 |
| IND10 | 26.471 | 5.495 | Multi-scan | low | 105,595 |
| GUY02 | 33.531 | 7.275 | Multi-scan | low | 143,861 |
| GUY09 | 36.517 | 10.557 | Multi-scan | low | 95,740 |
| S1 | 8.130 | 3.048 | single-scan | medium | 64,060 |
| S2 | 6.860 | 2.760 | single-scan | medium | 39,187 |
| S3 | 8.750 | 3.084 | single-scan | high | 25,664 |
| S4 | 6.620 | 3.207 | single-scan | high | 31,586 |

for the 29 tree samples, with satisfactory tree volume estimations. The same conclusions can be drawn from the concordance correlation coefficient, where the concordance correlation coefficient of SfQSM is significantly higher than that of the other two modeling methods.

This paper further calculated the volume deviations of these three tree modeling methods. The box plot of volume deviations of the 29 tree samples was shown in Fig. 9 (a). It is evident that the mean volume deviation of the proposed method is significantly lower than that of the other two methods. Furthermore, TreeQSM and AdQSM exhibit several extremely large volume deviations. For example, the largest volume deviation of TreeQSM approaches $-20$ m$^3$, while the largest volume deviation of AdQSM is close to 20 m$^3$. In contrast, most volume deviations of the proposed method are around zero. This indicates that the proposed method exhibits strong robustness across different tree samples. The kernel density function distribution of volume deviations for these three methods was also calculated and shown in Fig. 9 (b). It can be observed that most tree volume deviations of the proposed method are concentrated around zero, while the other two methods exhibit several extremely large tree volume deviations.

Additionally, this study calculated the coefficient of determination ($R^2$) for these three modeling methods, which is defined as Eqs. (12)–(14).

$$S_{reg} = \sum_{i=1}^{n} \left(V_i^f - \overline{V}\right)^2 \tag{12}$$

$$S_{tot} = \sum_{i=1}^{n} \left(V_i - \overline{V}\right)^2 \tag{13}$$

$$R^2 = S_{reg}/S_{tot} \tag{14}$$

where $V_i^f$ is the $i$-th fitted tree volume. $R^2$ reflects how closely the calculated tree volumes align with the harvested tree volumes. Fig. 9 (c) depicts the fitted lines between the calculated and harvested tree volumes for these three methods. Ideally, if the calculated tree volumes perfectly match the harvested tree volumes, all points in the figure

would lie along the 1:1 line. In this case, $R^2$ would be equal to 1. Therefore, a higher coefficient of determination closer to 1 indicates more accurate tree volume estimation results. From Fig. 9 (c), it can be observed that the proposed method achieved the highest coefficient of determination, indicating superior tree volume estimation results.

To visually demonstrate the modeling effects of different methods, this paper overlays the point cloud and modeling results, as shown in Fig. 10. The first column displays eight individual tree point clouds with selected zoomed-in areas. The second, third, and fourth columns present the corresponding modeling results of different methods (TreeQSM, AdQSM and SfQSM) for these areas. The first two rows depict the local modeling results for the main stems. It can be observed that TreeQSM tends to produce discontinuous cylinders, resulting in fragmented modeling results (Fig. 10 (a1) and (b1)). On the other hand, AdQSM has a tendency to over-fit branches, resulting in branch models that do not align well with the scanned point cloud. Additionally, AdQSM constructs branch models even where no tree points exist (Fig. 10 (b2)). In comparison, our proposed method produces accurate branch models that fit well with the point clouds. Fig. 10 (c)-(c3) and (d)-(d3) illustrate the modeling results for branches connected to tree canopies. TreeQSM incorrectly constructs branch models, especially for modeling result shown in Fig. 10 (c1). Regarding the points shown in Fig. 10 (d), AdQSM wrongly produced many non-existent branches as shown in Fig. 10 (d2). Similar findings can be observed in Fig. 10 (e2) and (h2), where AdQSM produces a large number of false branches. Fig. 10 (f)-(f3) show the modeling results for branches within the canopy. It is evident that the proposed method can produce the best modeling result with branch models distributed align with the branch points. Both Fig. 10 (e1) and (g1) indicate that TreeQSM tends to generate discontinuous branch models. In contrast, our proposed method obtains satisfactory branch models that align well with the branch points as shown in Fig. 10 (e3) and (g3).

## 4. Discussion

In general, tree samples scanned in multi-scan mode allow for the acquisition of a 'complete' set of individual tree points through co-registration of the multi-scanned point clouds. This reduces data gaps caused by single scanning views or self-occlusion. Conversely, tree samples scanned in single-scan mode generally encounter larger data gaps.

To discuss the robustness of the proposed method with trees exhibiting smaller or larger data gaps, both four individual trees scanned in single-scan mode and multi-scan mode were used for visualization of the modeling results. These eight individual tree points are shown in Fig. S1 (found in the Supplementary Materials), and detailed information is provided in Table 3.

Fig. S2 presents the modeling results of individual tree point clouds scanned in multi-scan mode. It is evident that TreeQSM performed the poorest compared to AdQSM and the proposed method. The TreeQSM modeling results exhibit numerous inaccurately fitted cylinders within the trunks (Fig. S2 (a), (b), and (d)). Additionally, TreeQSM fails to achieve satisfactory modeling results for branches within the canopy. This can be attributed to the heavy reliance of TreeQSM on the quality of individual tree point clouds. In cases where the point cloud quality is subpar, containing data gaps or outliers, TreeQSM yields unsatisfactory individual tree models. On the other hand, AdQSM produces significantly better individual tree modeling results, as illustrated in Fig. S2 (e), (f), and (h). AdQSM's models appear to be closer to reality. However, it is noticeable that AdQSM tends to model straight trunks, which is not reasonable when a trunk is bent. In comparison, the proposed method achieves higher fidelity in its modeling results. The tree trunk models bend in accordance with the tree trunk point cloud variations. Moreover, regarding branches within the canopy, AdQSM tends to generate numerous dense and small branches. Fig. S2 (g) reveals an abundance of dense branches within the canopy, which contradicts reality. Based on the tree point clouds shown in Fig. S1 (a)–(d), it can be concluded that the proposed method achieves superior individual tree modeling results for tree point clouds scanned in multi-scan mode.

Fig. S3 showcases the modeling results of individual tree point clouds scanned in single-scan mode. It can be observed that there are numerous fragmented branches within the TreeQSM modeling results. The topological connection of branches within the canopy is discontinuous. This is due to the presence of data gaps in the individually scanned tree points. As mentioned previously, the performance of TreeQSM heavily relies on the quality of point clouds. When an individual tree is scanned in single-scan mode, larger data gaps will exist due to limitations in the scanning view and self-collusion. Despite the poor quality of individual tree points, both AdQSM and the proposed method still achieve satisfactory modeling results, as shown in Fig. S3 (e)–(h) and (i)-(l). A similar observation is made that AdQSM tends to yield over-fitted modeling results, particularly for stems. The modeling results for some curving branches appear excessively straight, deviating from the real scene. In contrast, the proposed method obtains satisfactory individual tree modeling results even when the tree points have larger data gaps.

Based on the previous discussion and analysis, both AdQSM and the proposed method (SfQSM) tend to achieve better results in individual tree modeling. In order to further compare the extraction results of skeleton lines, this study presents results (Fig. S4 and Fig. S5) showing the skeleton lines extracted for main stems from four multi-scanned individual tree points and four single-scanned individual tree points. From Fig. S4, it is evident that AdQSM produces over-fitted skeleton lines. These lines are unnaturally straight and fail to capture stem details, particularly in the case of curved stems, as indicated by the rectangular areas in Fig. S4 (a) and (d). Comparatively, the proposed method yields better results. The extracted skeleton lines conform well to the stem points and accurately depict the bending of branches. This can be attributed to two factors. Firstly, this study applies skeleton point adjustment and optimization, which centralizes the skeleton points within each point set. Secondly, it corrects the edge weight between two skeleton points as the closest distance among the corresponding contracted point sets. This edge weight setting helps preserve stem topology and prevents incorrect connections between skeleton nodes, which is more effective than using Euclidean distance or squared Euclidean distance as edge weights. In terms of the individual tree points scanned in single-scan mode, despite lower point density and larger data gaps, the proposed method is capable of accurately extracting skeleton lines that fit well with curved stems, as shown in Fig. S5. Conversely, AdQSM produces over-fitted skeleton lines that fail to capture branch details, particularly in Fig. S5 (c) and (d).

However, it must be acknowledged that the proposed method still struggles to perform effectively when faced with complex branching connection topologies, especially in the case of coniferous trees with numerous tiny branches. Fig. S6 displays the modeling outcomes using the proposed method for two coniferous trees with abundant tiny branches. It is evident that while the proposed method can accurately depict the main branches, several of the smaller branches are omitted from the models when comparing them to the branch points, as illustrated in Fig. S6 (d) and (h). This issue can be attributed to two main factors. Firstly, this study employed a Laplacian-based contraction technique to derive skeleton points, which tends to merge adjacent twigs into the same region, thereby failing to capture intricate structural details and resulting in some twig skeleton points not being extracted. Additionally, the study introduced a fractal self-similarity optimization approach for individual tree modeling. Unfortunately, some tiny branches were incorrectly identified as artificial branches and subsequently removed. Ensuring the preservation of structural details when encountering an abundance of tiny branches will be a key focus of our future research efforts.

## 5. Conclusion

Individual tree modeling using LiDAR point clouds is an important issue for forest ecology applications. However, building an accurate individual tree model remains challenging. This paper made three main contributions: proposing a skeleton points adjusting and optimization method to centralize the skeleton points, presenting a novel edge weight definition to extract realistic skeleton lines, and applying fractal self-similarity for optimizing the individual tree model.

To evaluate the modeling performance, the calculated tree volume based on the built individual tree model is compared with the referenced tree volume based on destructive harvest. The evaluation utilizes 29 individual tree points with corresponding harvested tree volumes. The proposed method achieves a mean deviation of 0.162 $m^3$ and a root mean square error of 1.023 $m^3$. The relative mean deviation and relative root mean square error are 0.01 % and 0.09 %, respectively. Furthermore, the concordance correlation coefficient of the proposed method is 0.994. These five accuracy indicators outperform those of two classical individual tree modeling methods, TreeQSM and AdQSM. Visual comparative analysis of eight selected individual trees showed that the proposed method achieved better modeling results regardless of whether the tree points were acquired in single-scan mode or multi-scan mode. The accuracy of skeleton lines extraction was also analyzed, and it was found that the extracted skeleton lines aligned well with tree points and were centralized within each point set. This can be attributed to two factors: firstly, adjusting and optimization techniques applied to initial skeleton points result in centralized skeleton points; secondly, edge weights are corrected using the closest distance among contracted point sets, leading to improved branch topological connection results. Furthermore, an ablation study is conducted to validate the effectiveness of the three main steps involved in this paper. The experimental results confirm the efficacy of each step.

The innovation of this study is not only found in the enhanced QSM construction performance resulting from the unique graph definition and fractal self-similarity optimization proposed, but also in its potential for various ecological applications. One example is its ability to directly support biodiversity assessments. Through the creation of precise individual tree models, this method can offer a detailed and dependable foundation for tree species classification and habitat analysis. Additionally, the precise QSM construction results can aid in accurate tree volume calculations, which are essential for estimating carbon stocks and understanding forest carbon cycles.

To sum up, this paper presents a high-fidelity tree modeling method for individual tree modeling using LiDAR point clouds. The proposed method surpasses existing methods in terms of accuracy and produces accurate and intuitive modeling results. This research contributes to advancing individual tree modeling and broader ecological applications like biodiversity assessments and carbon stock estimations. Future research will focus on further refining the method to address highly intricate branching patterns, especially within coniferous species featuring numerous delicate branches.

## Author contributions

Zhenyang Hui: Conceptualization, Software, Methodology, and writing—original draft. Yating He: Visualization and Investigation. Shuanggen Jin: Supervision and Writing – review & editing. Wenbo Chen: Validation and Data curation. :Penggen Cheng Supervision and Writing – review & editing. Yao Yevenyo Ziggah: Writing – review & editing. All reviewed and edited the manuscript.

## Data Availability

The individual trees TLS point clouds and destructive harvest tree volumes used for this research can be accessed at https://data.4tu.nl/articles/_/21552084. These datasets are provided by de Tanago (2018). The datasets are free to download and available for any use as long as the proper reference, as specified in the portal, is applied.

The source codes can be accessed at https://github.com/Smart3DLiDAR/SfQSM.

## Funding

This work was supported by the Funding of National Key Laboratory of Uranium Resources Exploration-Mining and Nuclear Remote Sensing (2024QZ-TD-26), Outstanding Young Talents Funding of Jiangxi Province (20232ACB213017), Double Thousand Plan of Jiangxi Province (DHSQT42023002), National Natural Science Foundation of China (NSF) (42161060, 41801325) and the Natural Science Foundation of Jiangxi Province (20242BAB25176, 20192BAB217010) for their financial support.

## Declaration of competing interest

The authors declare that they have no known competing financial interests or personal relationships that could have appeared to influence the work reported in this paper.

## Supplementary materials

The Figs. S1–S6.

## Appendix A. Supplementary data

Supplementary data to this article can be found online at https://doi.org/10.1016/j.plaphe.2025.100060.

## References

[1] X. Liang, J. Hyyppä, H. Kaartinen, M. Lehtomäki, J. Pyörälä, N. Pfeifer, M. Holopainen, G. Brolly, F. Pirotti, J. Hackenberg, et al., International benchmarking of terrestrial laser scanning approaches for forest inventories, ISPRS J. Photogrammetry Remote Sens. 144 (2018) 137–179.
[2] Q. Song, C.M. Albrecht, Z.T. Xiong, X.X. Zhu, Biomass estimation and uncertainty quantification from tree height, IEEE J. Sel. Top. Appl. Earth Obs. Rem. Sens. 16 (2023) 4833–4845.
[3] Y. Wang, J. Pyörälä, X. Liang, M. Lehtomäki, A. Kukko, X. Yu, H. Kaartinen, J. Hyyppä, In situ biomass estimation at tree and plot levels: what did data record and what did algorithms derive from terrestrial and aerial point clouds in boreal forest, Rem. Sens. Environ. 232 (2019) 111309.
[4] Z. Su, S. Li, H. Liu, Y. Liu, Extracting wood point cloud of individual trees based on geometric features, Geosci. Rem. Sens. Lett. IEEE 16 (8) (2019) 1294–1298.
[5] S. Li, L. Dai, H. Wang, Y. Wang, Z. He, S. Lin, Estimating leaf area density of individual trees using the point cloud segmentation of terrestrial LiDAR data and a Voxel-Based model, Remote Sens. 9 (11) (2017) 1202.
[6] X. Shen, L. Cao, N.C. Coops, H.C. Fan, X.Q. Wu, H. Liu, G.B. Wang, F.L. Cao, Quantifying vertical profiles of biochemical traits for forest plantation species using advanced remote sensing approaches, Rem. Sens. Environ. 250 (2020) 112041.
[7] Q. Ma, J. Lin, Y. Ju, W. Li, L. Liang, Q. Guo, Individual structure mapping over six million trees for New York City USA, Sci. Data 10 (1) (2023) 102.
[8] H. Weiser, J. Schäfer, L. Winiwarter, N. Krasovec, F.E. Fassnacht, B. Höfle, Individual tree point clouds and tree measurements from multi-platform laser scanning in German forests, Earth Syst. Sci. Data 14 (7) (2022) 2989–3012.
[9] Q. Guo, Y. Su, T. Hu, H. Guan, S. Jin, J. Zhang, X. Zhao, K. Xu, D. Wei, M. Kelly, et al., Lidar boosts 3D ecological observations and modelings: a review and perspective, IEEE Geosci. Rem. Sens. Magaz. 9 (1) (2021) 232–257.
[10] Z. Hui, Z. Cai, B. Liu, D.J. Li, H. Liu, Z. Li, A Self-Adaptive optimization individual tree modeling method for terrestrial LiDAR point clouds, Remote Sens. 14 (11) (2022) 2545.
[11] Y. Liu, J. Guo, B. Benes, O. Deussen, X. Zhang, H. Huang, TreePartNet: neural decomposition of point clouds for 3D tree reconstruction, ACM Trans. Graph. 40 (6) (2021) 1–6.
[12] D. Kükenbrink, O. Gardi, F. Morsdorf, E. Thürig, A. Schellenberger, L. Mathys, Above-ground biomass references for urban trees from terrestrial laser scanning data, Ann. Bot. 128 (6) (2021) 709–724.
[13] B. Brede, L. Terryn, N. Barbier, H.M. Bartholomeus, R. Bartolo, K. Calders, G. Derroire, S. Moorthy, A. Lau, S.R. Levick, et al., Non-destructive estimation of individual tree biomass: allometric models, terrestrial and UAV laser scanning, Rem. Sens. Environ. 280 (2022) 113180.
[14] K. Cálders, G. Newnham, A. Burt, S. Murphy, P. Raumonen, M. Herold, D. Culvenor, V. Avitabile, M. Disney, J. Armston, et al., Nondestructive estimates of

above-ground biomass using terrestrial laser scanning, Methods Ecol. Evol. 6 (2) (2015) 198–208.
[15] L.J. Cárdenas, A. López, J.C. Ogayar, R.F. Feito, M.J. Jurado, Reconstruction of tree branching structures from UAV-LiDAR data, Front. Environ. Sci. 10 (2022) 960083.
[16] B. Brede, K. Calders, A. Lau, P. Raumonen, H.M. Bartholomeus, M. Herold, L. Kooistra, Non-destructive tree volume estimation through quantitative structure modelling: comparing UAV laser scanning with terrestrial LIDAR, Rem. Sens. Environ. 233 (2019) 111355.
[17] J.G. de Tanago, A. Lau, H. Bartholomeus, M. Herold, V. Avitabile, P. Raumonen, C. Martius, R.C. Goodman, M. Disney, S. Manuri, et al., Estimation of above-ground biomass of large tropical trees with terrestrial LiDAR, Methods Ecol. Evol. 9 (2) (2018) 223–234.
[18] M. Demol, K. Calders, H. Verbeeck, B. Gielen, Forest above-ground volume assessments with terrestrial laser scanning: a ground-truth validation experiment in temperate, managed forests, Ann. Bot. 128 (6) (2021) 805–819.
[19] S. Momo Takoudjou, P. Ploton, B. Sonké, J. Hackenberg, S. Griffon, F. de Coligny, N.G. Kamdem, M. Libalah, G.I. Mofack, G. Le Moguédec, et al., Using terrestrial laser scanning data to estimate large tropical trees biomass and calibrate allometric models: a comparison with traditional destructive approach, Methods Ecol. Evol. 9 (4) (2018) 905–916.
[20] M. Åkerblom, P. Raumonen, R. Mäkipää, M. Kaasalainen, Automatic tree species recognition with quantitative structure models, Rem. Sens. Environ. 191 (2017) 1–12.
[21] Z.Y. Hui, Z.C. Cai, P. Xu, Y.P. Xia, P.G. Cheng, Tree species classification using optimized features derived from light detection and ranging point clouds based on fractal geometry and quantitative structure model, Forests 14 (6) (2023) 1265.
[22] X. Shen, L. Cao, Y.S. Ma, N.C. Coops, E.R. Muise, G.B. Wang, F.L. Cao, Estimating structure of understory bamboo for giant panda habitat by developing an advanced vertical vegetation classification approach using UAS-LiDAR data, Int. J. Appl. Earth Obs. Geoinf. 136 (2025) 104304.
[23] G.P. Fan, L.L. Nan, Y.Q. Dong, X.H. Su, F.X. Chen, AdQSM: a new method for estimating Above-Ground biomass from TLS point clouds, Remote Sens. 12 (18) (2020) 3089.
[24] X.L. Liang, V. Kankare, X.W. Yu, J. Hyyppä, M. Holopainen, Automated stem curve measurement using terrestrial laser scanning, IEEE Trans. Geosci. Rem. Sens. 52 (3) (2014) 1739–1748.
[25] D. Wang, M. Hollaus, E. Puttonen, N. Pfeifer, Automatic and Self-Adaptive stem reconstruction in Landslide-Affected forests, Remote Sens. 8 (12) (2016) 974.
[26] S.L. Du, R. Lindenbergh, H. Ledoux, J. Stoter, L.L. Nan, AdTree: accurate, detailed, and automatic modelling of Laser-Scanned trees, Remote Sens. 11 (18) (2019) 2074.
[27] H. Tang, S. Li, Z. Su, Z. He, Cluster-Based wood–leaf separation method for forest plots using terrestrial laser scanning data, Remote Sens. 16 (18) (2024) 3355.
[28] H. Xu, N. Gossett, B.Q. Chen, Knowledge and heuristic-based modeling of laser-scanned trees, ACM Trans. Graph. 26 (4) (2007) 19.
[29] S. Delagrange, C. Jauvin, P. Rochon, PypeTree: a tool for reconstructing tree perennial tissues from point clouds, Sensors (Peterb., NH) 14 (3) (2014) 4271–4289.
[30] P. Raumonen, M. Kaasalainen, M. Åkerblom, S. Kaasalainen, H. Kaartinen, M. Vastaranta, M. Holopainen, M. Disney, P. Lewis, Fast automatic precision tree models from terrestrial laser scanner data, Remote Sens. 5 (2) (2013) 491–520.
[31] J. Hackenberg, H. Spiecker, K. Calders, M. Disney, P. Raumonen, SimpleTree —an efficient open source tool to build tree models from TLS clouds, Forests 6 (11) (2015) 4245–4294.
[32] D.M. Yan, J. Wintz, B. Mourrain, W.P. Wang, F. Boudon, C. Godin, Efficient and robust reconstruction of botanical branching structure from laser scanned points. The 11th IEEE International Conference on Computer-Aided Design and Computer Graphics, IEEE, Huangshan, China, 2009 Aug 19-21.
[33] R.H. Li, G.C. Bu, P. Wang, An automatic tree skeleton extracting method based on point cloud of terrestrial laser scanner, Int. J. Opt. 2017 (2017) 1–11.
[34] M.Y. Ai, Y. Yao, Q.W. Hu, Y. Wang, W. Wang, An automatic tree skeleton extraction approach based on Multi-View slicing using terrestrial LiDAR scans data, Remote Sens. 12 (22) (2020) 3824.
[35] Z.Y. Hui, Z.X. Li, S.G. Jin, B. Liu, D.J. Li, Street tree extraction and segmentation from mobile LiDAR point clouds based on spatial geometric features of object primitives, Forests 13 (8) (2022) 1245.
[36] J.T. Li, H.B. Wu, Z.H. Xiao, H.Q. Lu, 3D modeling of laser-scanned trees based on skeleton refined extraction, Int. J. Appl. Earth Obs. Geoinf. 112 (2022) 102943.
[37] X. Li, X. Zhou, S. Xu, Individual tree reconstruction based on circular truncated cones from portable LiDAR scanner data, Geosci. Rem. Sens. Lett. IEEE 20 (2023) 1–5.
[38] O.K. Au, C. Tai, H. Chu, D. Cohen-Or, T. Lee, Skeleton extraction by mesh contraction, ACM Trans. Graph. 27 (3) (2008) 1–10.
[39] J.J. Cao, A. Tagliasacchi, M. Olson, H. Zhang, Z.X. Su, Point cloud skeletons via laplacian based contraction. 2010 Shape Modeling International Conference, IEEE, Aix-en-Provence, France, 2010 Jun 21-23.
[40] Z.X. Su, Y.D. Zhao, C.J. Zhao, X.Y. Guo, Z.Y. Li, Skeleton extraction for tree models, Math. Comput. Model. 54 (3–4) (2011) 1115–1120.
[41] Z. Wang, L.Q. Zhang, T. Fang, P.T. Mathiopoulos, H.M. Qu, D. Chen, Y.B. Wang, A Structure-Aware global optimization method for reconstructing 3-D tree models from terrestrial laser scanning data, IEEE Trans. Geosci. Rem. Sens. 52 (9) (2014) 5653–5669.
[42] J.Z. Xu, J. Shan, G. Wang, Hierarchical modeling of street trees using mobile laser scanning, Remote Sens. 12 (14) (2020) 2321.
[43] B.X. Wu, G. Zheng, Y. Chen, D.S. Yu, Assessing inclination angles of tree branches from terrestrial laser scan data using a skeleton extraction method, Int. J. Appl. Earth Obs. Geoinf. 104 (2021) 102589.
[44] J.Q. Sun, P. Wang, R.H. Li, M. Zhou, Y.H. Wu, Fast tree skeleton extraction using voxel thinning based on tree point cloud, Remote Sens. 14 (11) (2022) 2558.
[45] M. Ester, H. Kriegel, J.O.R. Sander, X.W. Xu, A density-based algorithm for discovering clusters in large spatial databases with noise. KDD'96: Proceedings of the Second International Conference on Knowledge Discovery and Data Mining, AAAI Press, Portland, Oregon, 1996 Aug 2.
[46] Y. Livny, F. Yan, M. Olson, B.Q. Chen, H. Zhang, J. El-Sana, Automatic reconstruction of tree skeletal structures from point clouds, ACM Trans. Graph. 29 (6) (2010) 1–8.
[47] B.B. Mandelbrot, The fractal geometry of nature/B.B. Mandelbrot, Am. J. Phys. 51 (3) (1983) 286.
[48] Q.J.A. Guzmán, S. Iain, A. Felipe, G.A. Sánchez-Azofeifa, On the relationship of fractal geometry and tree-stand metrics on point clouds derived from Terrestrial Laser Scanning, Methods Ecol. Evol. 11 (10) (2020) 1309–1318.
[49] E.M. Nogueira, B.W. Nelson, P.M. Fearnside, Wood density in dense forest in central Amazonia, Brazil, For. Ecol. Manag. 208 (1) (2005) 261–286.